



# Post-heat treatment effect on dielectric and optical properties of magnesium-based spinel

Prabhpreet Kaur<sup>1</sup> · Suman Rani<sup>1</sup>

Received: 27 October 2023 / Accepted: 18 December 2023 / Published online: 30 January 2024  
© The Author(s), under exclusive licence to Springer Science+Business Media, LLC, part of Springer Nature 2024

## Abstract

The current work reports the synthesis of magnesium aluminate spinel ( $\text{MgAl}_2\text{O}_4$ ) using wet-chemical sol-gel technique at two different sintering temperatures of 900 °C and 1100 °C. The crystal structure of  $\text{MgAl}_2\text{O}_4$  at both sintering temperatures was confirmed by X-ray diffraction. The obtained results showed the successful formation of  $\text{MgAl}_2\text{O}_4$  along with some impurity peaks of magnesium oxide. Here, the crystallite size shows the linear nature with sintering temperature. The field emission scanning electron microscope (FESEM) shows the spherical shape. The change in morphology with sintering temperature is also confirmed by FESEM. Optical and electronic responses were studied by Fluorescence (FL) and electrochemical impedance spectroscopy (EIS). The FL study reveals that the prepared nanopowder tends to emit white light under the excitation wavelength of 350 nm. The intensity of emission peaks has been found to increase with sintering temperature, indicating an increase in defect states. Furthermore, using EIS data, the electrical parameters were studied in pellet form in the frequency range of 1 to  $10^6$  Hz. The Nyquist plots have been successfully explained by employing LR[Q[R(CR)]] equivalent circuit corresponding to grain, grain boundary, and electrode contribution. The examined parameters have been significantly influenced by the sintering temperature. An increase in temperature is observed to result in higher values for the dielectric constant, loss tangent, and conductivity. Additionally, the electric modulus spectra reveal non-Debye behavior in the samples. The obtained results reveal that the prepared nanopowder can be used in optoelectronic devices, high-frequency equipment, and high-storage media.

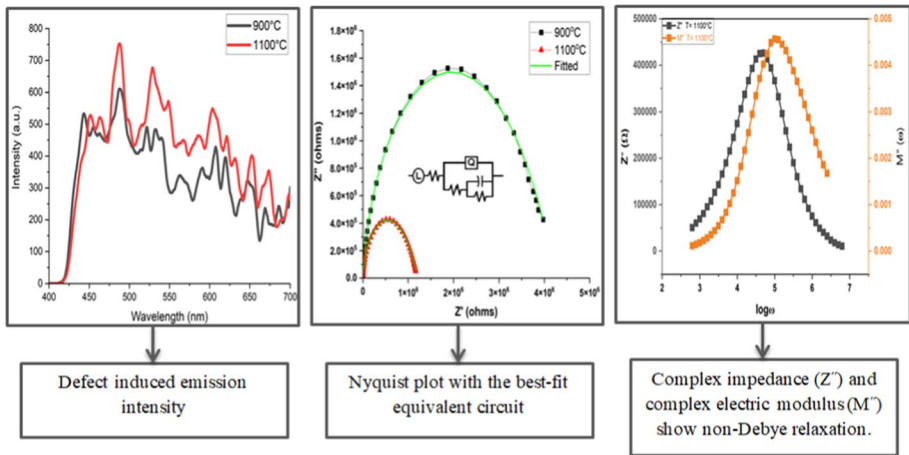
---

✉ Suman Rani  
suman.rani@lpu.co.in

Prabhpreet Kaur  
prabhpreetk89@gmail.com

<sup>1</sup> Department of Physics, School of Chemical Engineering and Physical Sciences, Lovely Professional University, Phagwara, Punjab 144411, India

## Graphical abstract



**Keywords** Sol-gel method · Magnesium aluminate spinel · Fluorescence · Impedance spectroscopy · Optoelectronic devices · Storage media

## 1 Introduction

Spinel materials, characterized by the general formula  $AB_2O_4$  (where A represents a divalent cation and B a trivalent cation), exhibit remarkable optical, electrical, and magnetic properties, making them valuable for various applications (Manohar et al. 2022; Mostafa et al. 2022; Shi et al. 2020; Sun et al. 2023). Among these, magnesium aluminate ( $MgAl_2O_4$ ) stands out due to its exceptional traits, including wide bandgap energy, insulating dielectric characteristics, high electrical resistivity, and its potential in device applications.

In its ideal form,  $MgAl_2O_4$  spinel comprises 32 oxygen ions within a single unit cell. Of these, 8 tetrahedral positions out of 64 are occupied by magnesium ions, while aluminum ions occupy 16 octahedral sites out of 32 (Shi et al. 2020). However, the presence of defects in the material can significantly impact its structural, optical, electrical, and dielectric properties (Ali et al. 2021). Oxygen vacancies, for instance, play a crucial role in determining the optical and dielectric characteristics of  $MgAl_2O_4$ , also enhancing its ionic conductivity (Rébola et al. 2013).

To explain the electrical properties of spinels, an analysis of complex impedance spectroscopy is vital. This technique involves the measurement of both real and imaginary parts of impedance across a range of frequencies. It serves as a vital tool for understanding the underlying conducting mechanisms and electrical properties by discriminating the contributions of grain, grain boundary, and grain electron effects (Jameel et al. 2023a, b, c; Panda and Behera 2014).

Previous studies have examined the impact of doping with elements such as Li, Ti, and  $Eu^{3+}$  on  $MgAl_2O_4$  spinels, revealing significant improvements in properties such as quality factor ( $Q_f$ ), mechanical strength, and luminescent responses. Notably, these studies have highlighted  $MgAl_2O_4$  potential in applications ranging from enhanced microwave

dielectric properties to the production of artificial red light in red LEDs (Li et al. 2023; Jian and Wen 2020; Rao et al. 2023).

In this context, this study investigates the synthesis of  $\text{MgAl}_2\text{O}_4$  using the wet chemical sol-gel method at different sintering temperatures. Surprisingly, to the best of our knowledge, there is a lack of studies regarding the influence of 900 °C and 1100 °C sintering temperature on the optical and dielectric properties of  $\text{MgAl}_2\text{O}_4$ . This paper, therefore, aims to bridge this gap by exploring how sintering temperature impacts the material on its structural, optical, and dielectric properties, thereby identifying potential application areas for this versatile material. The study employs various analytical techniques, including XRD, FTIR (Fourier-transform Infrared), and FESEM, to assess structural impacts. Optical properties are examined through FL, while EIS is utilized for dielectric studies.

## 2 Materials and methods

A wet chemical sol-gel method was adopted to prepare magnesium aluminate spinel ( $\text{MgAl}_2\text{O}_4$ ) using magnesium nitrate [ $\text{Mg}(\text{NO}_3)_2 \cdot 6\text{H}_2\text{O}$ ] with 98% purity, aluminum nitrate [ $\text{Al}(\text{NO}_3)_3 \cdot 9\text{H}_2\text{O}$ ] with 98% purity, ammonia solution [ $\text{NH}_4\text{OH}$ ] with 25% AR quality, citric acid ( $\text{C}_6\text{H}_8\text{O}_7 \cdot \text{H}_2\text{O}$ ) with purity of 98% all sourced from LOBA company as precursors. The magnesium nitrate and aluminum nitrate were weighed accordingly and dissolved in 100 ml of distilled water each for 30 min in two separate beakers on a stirrer. After 30 min, these solutions were mixed in one beaker maintaining the heating temperature at 80 °C to make a homogenous clear solution. After 3 h, citric acid was mixed into the solution (by weighting the metal-to-citric ratio as 1:1) which acts as a chelating agent. Next drop wise ammonia was added to the solution to keep the pH7. This solution was stirred and heated until it became viscous and a xerogel was formed. This gel was dried on a hot plate and then in a hot air oven to obtain the material in powder form. Finally, the prepared powder was sintered at 900 °C and 1100 °C in a muffle furnace for further studies. The preparation method is represented systematic diagram as shown in Fig. 1.

## 3 Structural Studies

### 3.1 XRD

Figure 2 shows the XRD pattern of  $\text{MgAl}_2\text{O}_4$  nanoparticles sintered at 900 °C and 1100 °C for 4 h. The XRD peaks show the cubic spinel-type structure of pure  $\text{MgAl}_2\text{O}_4$  with diffraction peaks at 31.2°, 36.8°, 44.7°, 55.7°, 59.4°, and 65.2° (Joint Committee on Powder Diffraction Standards (JCPDS) file 00-021-1152) having space group  $\text{Fd}3\text{m}$  and two diffraction peaks of MgO phase were also observed. The stoichiometric ratio of the formed spinel is 1:2 with an impurity phase of MgO. The presence of the MgO phase indicates that there was an excess of magnesium in the starting composition. The intensity of diffraction peaks increases with sintering temperature which indicates the increase in the crystalline nature of the material. As the peak intensity increases, full-width half maxima decrease which increases in crystallite size. The crystallite size (D) is calculated using (Kaur and Rani 2023):

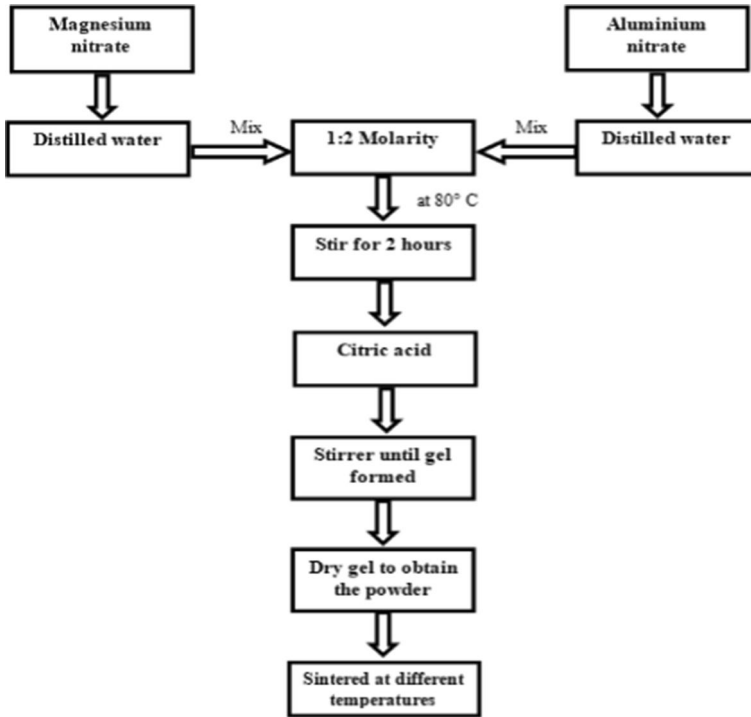


Fig. 1 Schematic diagram showing the mechanism of prepared samples

$$D = \frac{0.94\lambda}{\beta \cos\theta} \tag{1}$$

The lattice constant (a) was calculated using the following equation

$$a = \frac{\lambda}{2} \frac{\sqrt{h^2 + l^2 + k^2}}{\sin\theta} \tag{2}$$

$\lambda$  is wavelength, hkl are corresponding Miller indices, and  $\theta$  is diffraction angle. All the values are tabulated in Table 1. The X-ray density ( $\rho$ ), bulk density ( $\rho_o$ ), and porosity (V) of the material are also calculated using the following equations (Ahmed et al. 2022; Zayani et al. 2021):

$$\rho_o = \frac{m}{\pi r^2 h}, \rho = \frac{8M}{NV}, V = \left(1 - \frac{\rho_o}{\rho}\right) \tag{3}$$

where m is the mass; h is the thickness of the pellet; M is molar mass; N is Avogadro’s number; V is the volume of the unit cell ( $a^3$ ) (Jameel et al. 2023a, b, c; Saleem et al. 2022a, b, c). The calculated value of X-ray density increases by increasing the sintering temperature. On the other hand, the value of bulk density is smaller than X-ray density which indicates the existence of pores in the sample. The value of porosity (V) decreases with the increase in sintering temperature, shown in Figs. 2 and 3, due to the effect of impurity

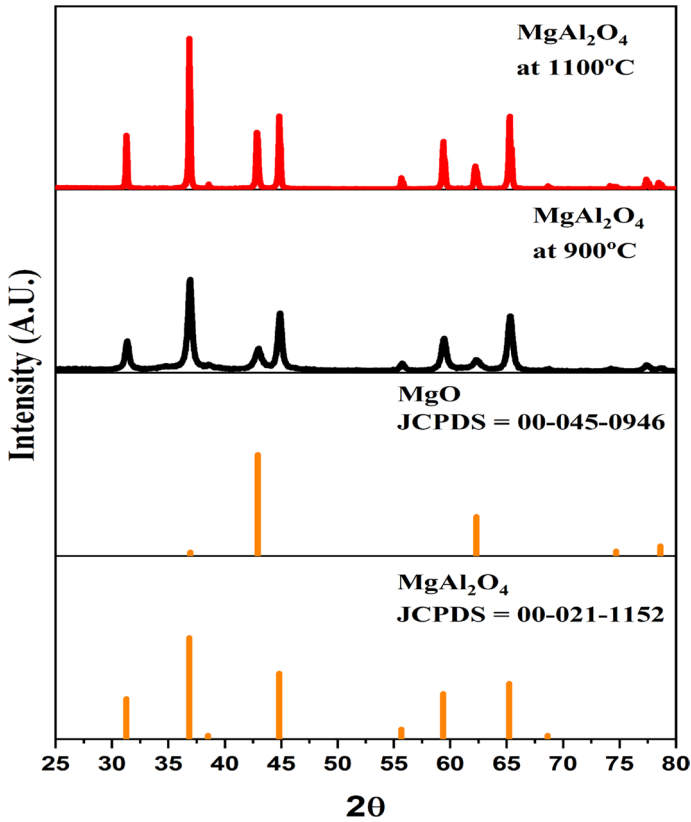


Fig. 2 XRD analysis of  $\text{MgAl}_2\text{O}_4$

**Table 1** Structural parameters for  $\text{MgAl}_2\text{O}_4$  at different sintering temperatures

Parameters	900 °C	1100 °C
Peak Intensity (degree)	30.77	164.59
Crystallite size (D, nm)	22.19	49.42
Lattice constant (a, Å)	8.07	8.06
X-ray density ( $\rho_x$ , g/cm <sup>3</sup> )	3.57	3.57
Bulk density ( $\rho_m$ , g/cm <sup>3</sup> )	0.15	0.22
Porosity (V)	0.89	0.84

or intrinsic defects in the material (Thibaudeau and Gervais 2002; Jagadeeshwaran et al. 2018).

### 3.2 Fourier transform infrared (FTIR)

The FTIR spectra presented depicted in Fig. 4 within the wavenumber range of 400–4000  $\text{cm}^{-1}$  provide valuable insights into the structural formation and coordination

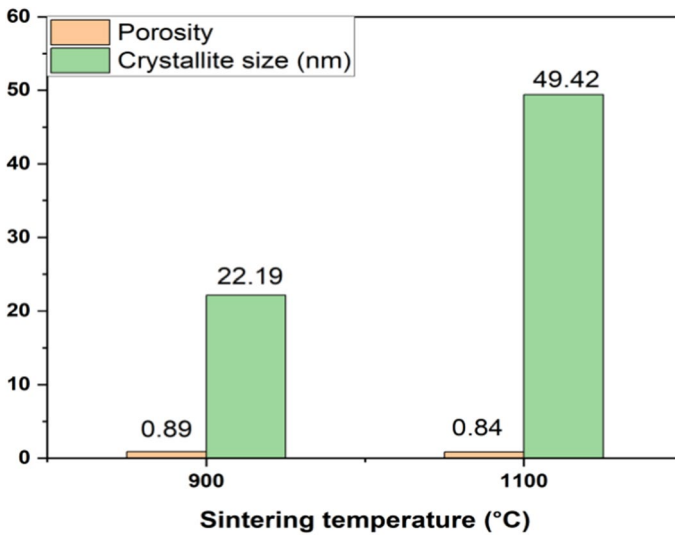
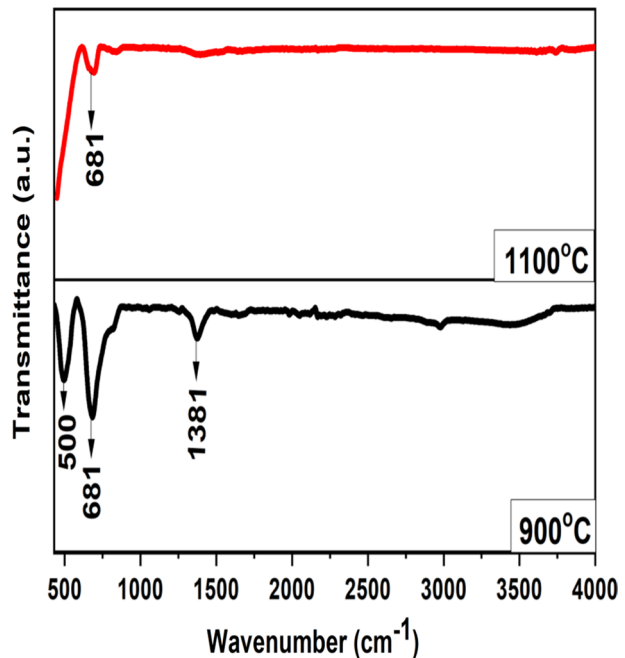


Fig. 3 Illustrating the relation of porosity and crystallite size with sintering temperature  $\text{MgAl}_2\text{O}_4$

Fig. 4 FTIR analysis of  $\text{MgAl}_2\text{O}_4$



states of Al and Mg cations during the synthesis of nanocrystalline spinel phase  $\text{MgAl}_2\text{O}_4$ . The analysis of the spectra at different temperatures reveals significant information about the chemical bonds. At 900 °C, a distinct peak at 1381  $\text{cm}^{-1}$  signifies N–O (nitrates) vibrations, which diminish as the temperature increases. Alongside, peaks at 681  $\text{cm}^{-1}$  and 500  $\text{cm}^{-1}$  emerge, indicating the formation of  $\text{MgAl}_2\text{O}_4$  spinel. During 900 °C, some

impurity peaks are apparent; however, these impurities diminish as the temperature rises. At higher temperatures, i.e., at 1100 °C only metal–oxygen–metal peaks of Mg–O–Al bonds appeared which successfully confirms the formation of MgAl<sub>2</sub>O<sub>4</sub> spinel.

Across varying temperatures (900 °C and 1100 °C), the consistent observation of metal–oxygen–metal bonds within the 500–800 cm<sup>-1</sup> range affirms the structural stability of MgAl<sub>2</sub>O<sub>4</sub> spinel. The vibrational bands in this spectral region clarify the spinel-type structure, clarifying lattice vibrations originating from tetrahedral and octahedral coordinated metal ions (Rao et al. 2023). Vibrations in the 500–800 cm<sup>-1</sup> range correspond to the vibrational Al–O bonds of the octahedral site and the network vibrations of Mg–O bonds inherent in normal spinel (Barik et al. 2011; Hinklin and Laine 2008).

The complete confirmation of MgAl<sub>2</sub>O<sub>4</sub> spinel formation is improved by the combined analysis of XRD and FTIR spectra. The XRD data supplements the insights derived from FTIR by providing information on crystalline phases and their relative abundance. This dual analytical approach strengthens the confidence in the successful synthesis of nanocrystalline MgAl<sub>2</sub>O<sub>4</sub> spinel, offering a detailed understanding of its structural evolution under 900 °C, and 1100 °C sintering temperature.

### 3.3 FESEM

The surface characteristics of synthesized nanoparticles were investigated using FESEM analysis, as illustrated in Fig. 5a, b for MgAl<sub>2</sub>O<sub>4</sub> at 900 °C and 1100 °C. The FESEM images reveal the formation of a spherical shape also mentioned in the literature (Rao et al. 2023). It is observed that at 900 °C crystalline nature starts developing in the material. The grains are irregular in shape and with the increase of temperature, the shape of the crystallites was smooth and rounded, forming irregular structures. The grain size is analyzed in our prior work (Kaur and Rani 2023) which is 62 nm at 900 °C and 133 nm at 1100 °C. At lower temperature nucleation process decreases which prevent grain growth and causes agglomeration (Jameel et al. 2021a). As temperature rises, crystallites undergo sintering, leading to the formation of larger grains. Notably, increasing sintering temperature is associated with a decrease in porosity. Hence, when the temperature was increased from 900 up to 1100 °C, the rate of the nucleation process increased because of the existence of charges

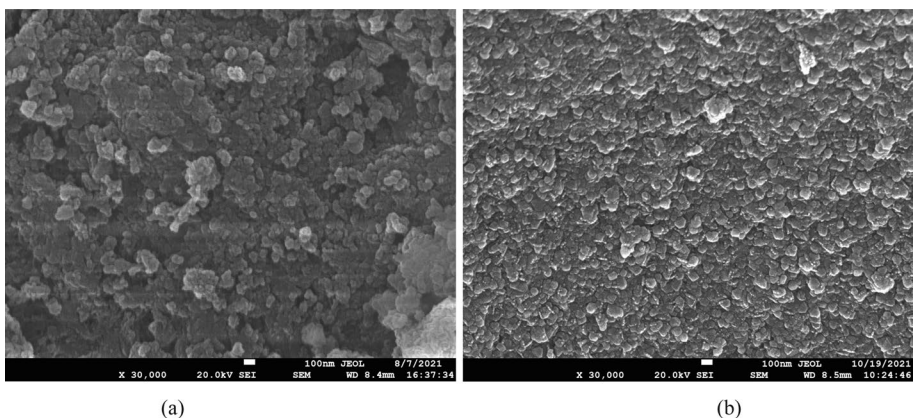


**Fig. 5** SEM images of MgAl<sub>2</sub>O<sub>4</sub> at (a) 900 °C (b) 1100 °C Refer to (Kaur and Rani 2023)

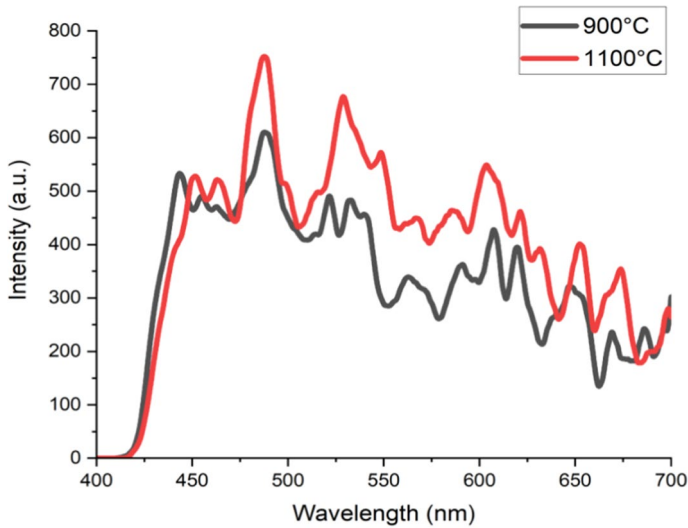


**Fig. 6** Displays the fluorescence emission spectra of  $\text{MgAl}_2\text{O}_4$

**Table 2** Defects centers responsible for emission wavelength

Dominating Emission wavelengths (nm)	Defects responsible for emission wavelength
460	Charge transfer between $\text{Al}^{3+}$ and $\text{O}^{2-}$
490	Trapping of the hole at Mg ion vacancy
525	Oxygen vacancy
540	F-centers
560	$\text{F}_2^{2+}$
610	Oxygen vacancy
680	$\text{F}_2^{1+}$

at the surface of the grains, and then agglomeration decreases due to a reduction in the number of cores and crystallinity also increases (Saleem et al. 2022c).

## 4 Luminescence studies

### 4.1 Fluorescence spectra

Figure 6 displays the fluorescence emission spectra of prepared samples of  $\text{MgAl}_2\text{O}_4$  at 900 °C and 1100 °C. The fluorescence spectra were taken with an excitation wavelength of 350 nm. The emission spectra of  $\text{MgAl}_2\text{O}_4$  at both temperatures are obtained in the visible region showing broad emission. The broad emission profile indicates that the compound reported in Table 2 has several emitting components that are responsible for broad emission profiles. In the graph, it is analyzed that the emission near 460 nm is caused by a charge transfer transition between the  $\text{Al}^{3+}$  ion and the  $\text{O}_2$  ions. The peak at 490 nm is due to an electron-to-hole transition trapped at the Mg ion vacancy. Oxygen vacancies are



the cause of the peak at 525 nm (Arun Kumar et al. 2021). Peaks at 540 nm are caused by F-centers. The octahedral  $\text{Al}^{3+}$  ion, which has two  $\text{F}^+$  centers, is surrounded by  $\text{F}_2^{2+}$  centers, and a peak at 610 nm is a result of oxygen vacancies brought on by the presence of MgAl antisites (Pathak et al. 2018). The existence of  $\text{F}_2^{1+}$  defect centers may be the cause of the peaks at 680 nm (Pathak et al. 2016). These multicolor emissions show the presence of multiple defect states inside the bandgap, each of which is caused by a different electronic transition. The intensity and integral area of this peak have been found to increase with sintering temperature, indicating an increase in defect states. This increase in the amount of defects also affects the conductivity of the material, which will be discussed in the next section.

## 5 Impedance analyses

Electrochemical Impedance Spectroscopy (EIS) is an effective experimental technique that examines a material's impedance properties using a small-amplitude alternating current (AC) signal. This method provides an impedance spectrum for the electrochemical substance being tested by measuring a system's impedance over a range of frequencies (Lazanas and Prodromidis 2023). By using this method the conductivity measurements of the prepared nanocrystalline  $\text{MgAl}_2\text{O}_4$  were analyzed. The powder was pressed in a KBr hydraulic press in the frequency range from 1 MHz to 1 Hz at 900 °C and 1100 °C. The measured impedance data were analyzed using 'Origin' and 'ZSimpWin' software.

Figure 7 shows the Nyquist plot (real  $Z'$  vs imaginary  $-Z''$ ) of nanocrystalline  $\text{MgAl}_2\text{O}_4$  powder. The observed impedance spectra of the  $\text{MgAl}_2\text{O}_4$  pellet show a semicircle in the measured frequency range. It is noticed that semicircles at both temperatures are slightly depressed instead of having centers on the real axis. This is a possibility due to the presence of grain orientation ( $R_g$ ), grain boundary ( $R_{gb}$ ), and electrode effect ( $R_{el}$ ). It should

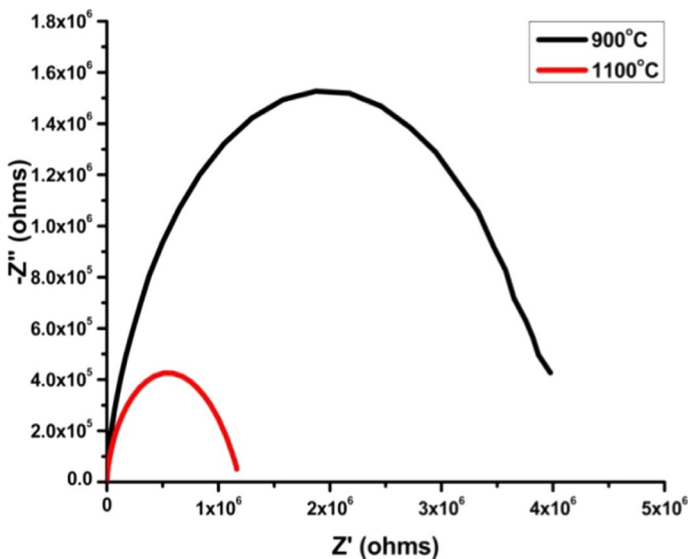


Fig. 7 Complex Impedance plot

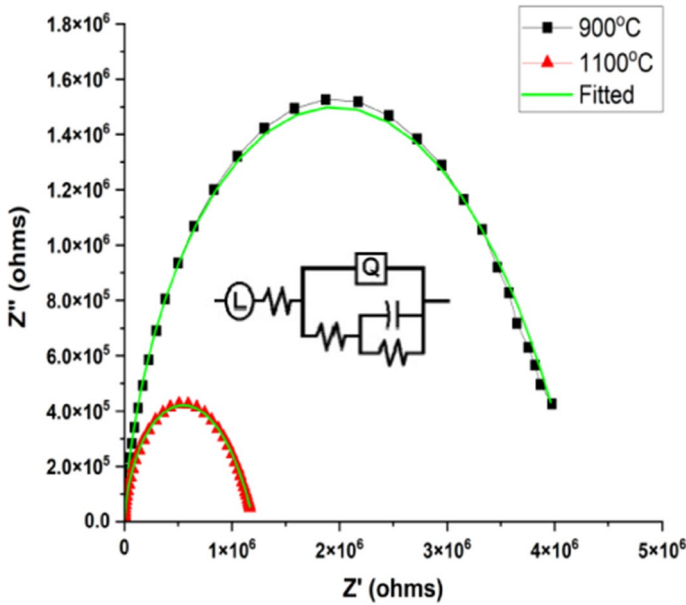


Fig. 8 Equivalent Circuit

Table 3 Simulated data of the electrical parameters

Parameters	At 900 °C		At 1100 °C	
	Start	End	Start	End
Inductance (μH)	1.00	4.71	1.00 E <sup>-6</sup>	3.06 E <sup>-7</sup>
Resistance, R <sub>g</sub> (MΩ)	0.36	0.01	2.98E <sup>5</sup>	8.10 E <sup>-9</sup>
CPE(μF)	1.00	1.97 E <sup>-3</sup>	1.00	3.93 E <sup>-3</sup>
Freq power, n	0.80	0.61	0.80	0.7352
Resistance [MΩ] [R <sub>gb</sub> ]	0.36	1.71	2.98 E <sup>5</sup>	9.745 E <sup>9</sup>
Capacitance [μF]	1.00	0.52	1.00	0.31
Resistance, Rel(MΩ)	0.36	4.31 E <sup>-3</sup>	2.98	9.74 E <sup>3</sup>

be noted that the absence of three separate semicircular arcs is because the grain, grain boundary, and electrode contributions are not far away (Hona et al. 2022; Mohan et al. 2016). Furthermore, the intercept of semicircles on the real axis (x-axis) shifts towards the higher frequency side with an increase in sintering temperatures. This indicates a negative temperature coefficient of resistance behavior of the material, like semiconductors (Mohan et al. 2016). It is noted that there is a decrease in curvature radius. This decrease in curvature radius can be attributed to the presence of non-Debye type behavior in the material (Joshi et al. 2017).

Furthermore, to analyze the effect of R<sub>g</sub>, R<sub>gb</sub>, and R<sub>el</sub>, the observed impedance spectra of MgAl<sub>2</sub>O<sub>4</sub> were fitted using ZSimp software and calculated its resistance and electrical behavior in the form of an equivalent electrical circuit. The best-fit equivalent circuit with typical fitting is depicted in Fig. 8 and Table 3, respectively. As shown in the table, the value of grain boundary resistance (R<sub>gb</sub>) is significantly higher than other resistance values

( $R_g$  and  $R_{cl}$ ). As can be seen, the value of resistance resulting from grain boundaries ( $R_{gb}$ ) increases by raising the sintering temperature from 900 to 1100 °C. These results are also well matched with FE-SEM data that as the sintering temperature increases, the crystallites sinter together and form larger grains with well-defined boundaries which contribute to the grain boundary resistance. Apart from resistance, for both models, a constant phase element (Q) is also included. The constant phase element is generally applied for the non-ideal capacitive behavior demonstrated by an imperfect semicircle. The nonideal behavior is caused by surface roughness, leakage capacitance, and non-uniform distribution (Hona et al. 2022). The impedance of a constant phase element is given by

$$Z(Q) = \frac{1}{C(i\omega)^n} \tag{4}$$

where  $\omega$  is the frequency and  $n$  is the frequency dispersion parameter related to the fractal dimension of the structure.

### 5.1 Real and imaginary impedance

The real and imaginary impedance of samples at 900 °C and 1100 °C is shown in Fig. 9. The real part of impedance represents the resistance to the flow of electrical current in the material. The imaginary part of impedance represents the reactance in the material. As seen, these real and imaginary impedance parts depend on the applied frequency.

As seen in real impedance, at the low-frequency region, the magnitude of the impedance ( $Z'$ ) is typically high. This means that the material resists the flow of electrical current at lower frequencies. As the frequency of the applied signal increases, the real part of the impedance decreases. The observed decreases in real impedance as the field frequency increases indicate that the material becomes more conductive (Costa et al. 2011; Joshi et al. 2017). This improved conductivity can be attributed to the relaxation of charge carriers. The insert graph shows the variation of  $Z''$  with frequency at 900 °C and 1100 °C

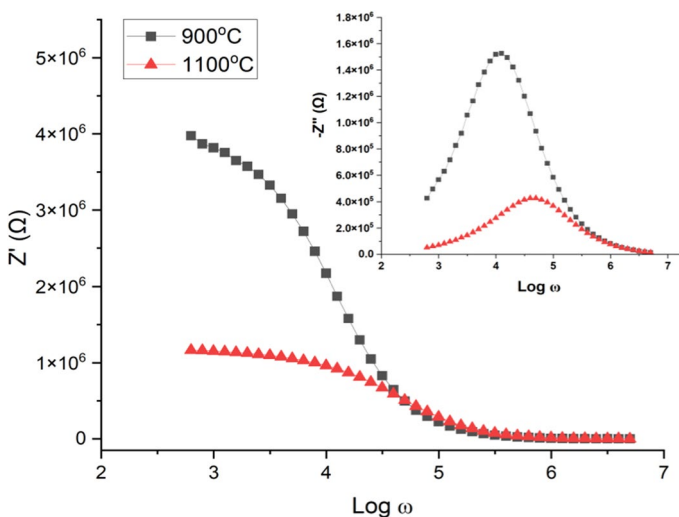


**Fig. 9** Real part of impedance (insert for the imaginary part of impedance)

temperatures. The spectra of  $Z''$  are characterized by the appearance of peaks that shift towards higher frequencies with increasing temperature. Such behavior indicates the existence of a relaxation phenomenon in the prepared material. The relaxation time ( $\tau$ ) is calculated using the following relation:

$$\tau = \frac{1}{2\pi f_{max}} \quad (5)$$

where  $f_{max}$  represents the relaxation frequency. The shifting of the peak towards a higher frequency region indicates that the value of  $\tau$  decreases with the rise in temperature, which suggests that the material is thermally activated.

The real and imaginary components of impedance ( $Z$ ) decrease with an increase in temperature in the low-frequency region. This implies that as the temperature increases the value of resistance and reactance decreases and hence the conductivity of the type material gets improved at higher temperatures i.e. at 1100 °C. On the other, the value of real and imaginary components of impedance ( $Z$ ) seems to merge in the high-frequency region. This means that at very high frequencies, the material behaves similarly, irrespective of temperature conditions.

## 5.2 A.C. conductivity ( $\sigma_{ac}$ )

Figure 10 shows the plot between  $\sigma_{ac}$  v/s  $\log \omega$  at two different temperatures. The a.c. conductivity of the sample was determined from the loss tangent by using the following relation (Joshi et al. 2017):

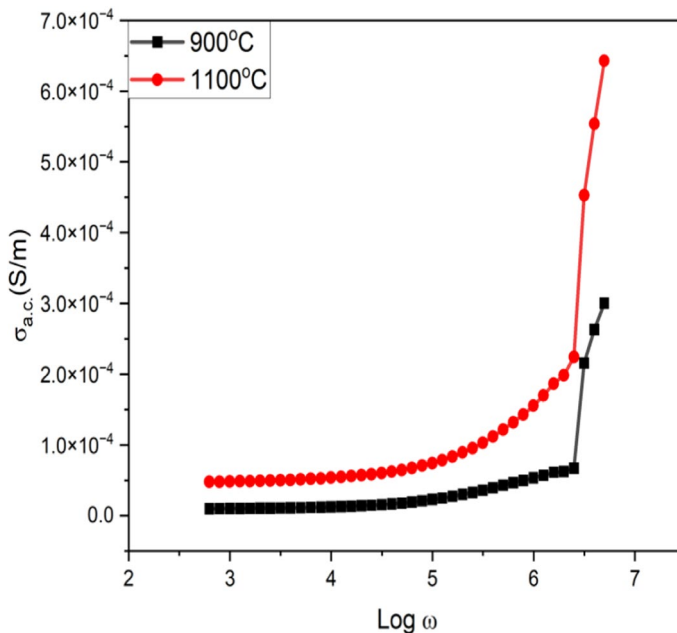


Fig. 10 Shows the plot between  $\sigma_{ac}$  v/s  $\log \omega$

$$\sigma_{a.c.} = \frac{t}{A} \cdot \frac{Z'}{Z'^2 + Z''^2} \tag{6}$$

where A is the cross-section area of the pellets, t is the thickness of pellet, Z' and Z'' are real and imaginary parts of impedance, respectively.

It is clear from Fig. 10 that by increasing the temperature, a.c. conductivity increases in the MgAl<sub>2</sub>O<sub>4</sub> sample. The reason for the increase in the a.c. conductivity of the sample is based on grain and grain boundary resistance inside a material. Moreover the presence of hopping mechanism of bound charges, in which, free charges hop back and forth between the well-defined bound states and hence, a.c. conductivity increases at higher frequencies.

According to Allah and Fayek (2000), in the spinel structure nanocrystalline MgAl<sub>2</sub>O<sub>4</sub> sample, the presence of Al<sup>3+</sup> ions in octahedral sites and Mg<sup>2+</sup> ions in tetrahedral sites is responsible for electric conduction due to the transfer of electrons between Al<sup>3+</sup> and Mg<sup>2+</sup> ions through hopping conduction mechanism. These charge carriers are not completely free but are strongly localized or displaced due to the effect of temperature. The transfer of charge carriers between the adjacent Mg<sup>2+</sup> occurs via O<sup>2-</sup> ions present in the system. The hopping of electrons between adjacent sites results in the local displacement of charges in the direction of the applied frequency. The local displacement of charge carriers increases with temperature and hence, conductivity increases with temperature. Another reason for the increase in alternating current (AC) conductivity, as the applied frequency increases, might be due to a reduction of porosity.

In Fig. 11, an Arrhenius plot was employed to depict the temperature-dependent electrical conductivity data across the range of 313–423 K. The derived activation energy (E<sub>a</sub>), determined from the slope of the Arrhenius plot, is recorded as 0.23 eV. This activation energy serves as a quantification of the energy barrier that charge carriers must surmount to traverse the material. The observed electrical conduction mechanism is attributed to the transfer of electrons between Al<sup>3+</sup> and Mg<sup>2+</sup> ions, characterized by a hopping conduction mechanism. Hopping conduction, established in materials where charge carriers navigate between localized states.

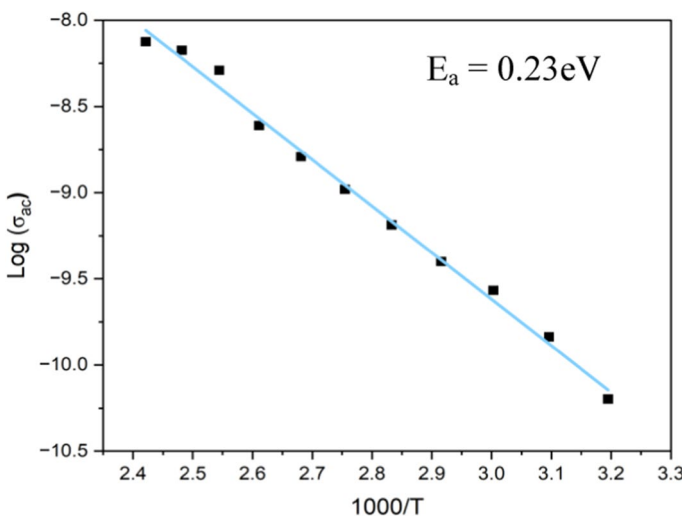


Fig. 11 Arrhenius plot at the temperature range of 313 to 423 K

The high goodness of fit value, specified as 0.9940, attests to the excellence of the Arrhenius model in describing the experimental data throughout the investigated temperature spectrum. This model fit underscores the robustness of the chosen model.

### 5.3 Dielectric permittivity and dielectric loss tangent

The complex dielectric function can be written as

$$\epsilon^* = \epsilon' - i\epsilon'' \tag{7}$$

where  $\epsilon'$  and  $\epsilon''$  denotes the real and imaginary part of dielectric constant. The real and imaginary components of the complex impedance are associated with dielectric permittivity and dielectric loss, respectively. This determines that the real part of complex dielectric illustrates the storage of energy, while imaginary part demonstrates the energy dissipation. In this study, the dielectric permittivity ( $\epsilon'$ ) and dielectric loss ( $\epsilon''$ ) along with dielectric loss tangent ( $\tan\delta$ ) is calculated using the expression (Justin and Rao 2010; Sharma et al. 2022):

$$\epsilon' = \frac{t}{\omega A \epsilon_0} \cdot \frac{Z''}{Z'^2 + Z''^2}, \epsilon'' = \frac{t}{\omega A \epsilon_0} \cdot \frac{Z'}{Z'^2 + Z''^2}, \tan\delta = \frac{\epsilon''}{\epsilon'} \tag{8}$$

where  $\epsilon_0$  is the permittivity of free space. Figure 12 shows the plot of dielectric permittivity ( $\epsilon'$ ) with applied frequency for the nanocrystalline  $MgAl_2O_4$  sample. It is noted from Fig. 12 that with the increase in applied frequency dielectric permittivity ( $\epsilon'$ ) decreases. In the low-frequency region, the ions do not flow which results in the pilings of charges. The periodic reversal of the applied field happens rapidly at high frequencies. As a result, there is no longer a piling of charges at the interface, and as a result, the dielectric constant decreases with frequency (Jamal et al. 2011).

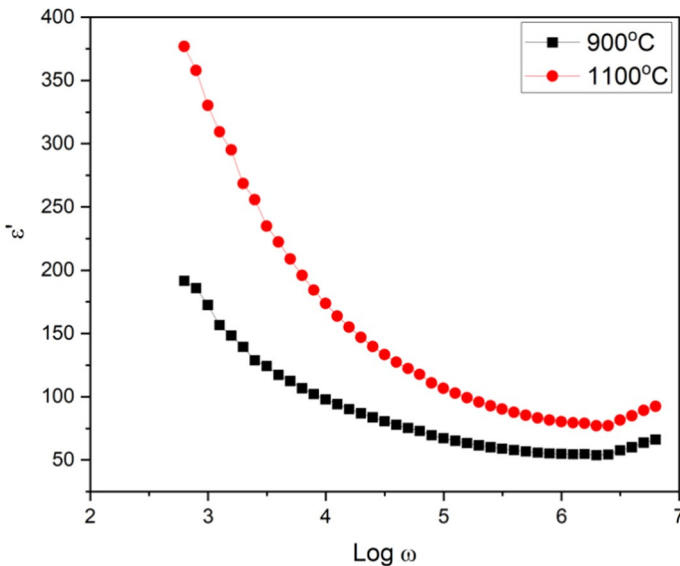


Fig. 12 Plot of dielectric permittivity ( $\epsilon'$ ) with applied frequency

The dielectric characteristics in spinel can be interpreted according to Koop's and Maxwell–Wagner's theory which states that the dielectric structure is mainly composed of highly conducting grains and rarely conducting grain boundaries, which are responsible for degree of polarization (Ali et al. 2021; Jameel et al. 2021a, b). When subjected to an externally applied field, charge carriers readily track the alternation in the electric field, accumulating at the interface on grain boundaries and resulting in interfacial polarization at lower frequencies. Conversely, at higher frequencies, charge carriers struggle to keep pace with the external electric field's changes due to which interfacial polarization inhibits resulting in a reduced dielectric constant with frequency. As mentioned in FESEM at higher temperature (1100 °C) defined grains are formed with more grain boundaries when compared to lower temperature. This leads to the conclusion that material has high value of dielectric constant at higher temperature. In addition, the charges in the  $\text{MgAl}_2\text{O}_4$  sample may have been thermally activated as the temperature increased, which results in the continuous increase in dielectric constant ( $\epsilon'$ ) with temperature.

Figure 13 shows the variation of dielectric loss tangent ( $\delta$ ) with applied frequency for the nanocrystalline  $\text{MgAl}_2\text{O}_4$  sample. From Fig. 13, it can be seen that the dielectric loss tangent decreases with the increase of applied frequency. As the temperature increases, the loss tangent increases, which may be due to the thermal activation and accumulation of charge carriers (Jamal et al. 2011). Another reason for the high value of dielectric loss might be due to defects. Imperfections in the material increase at higher temperatures and consequently the value of  $\tan\delta$  increases (Mohan et al. 2016).

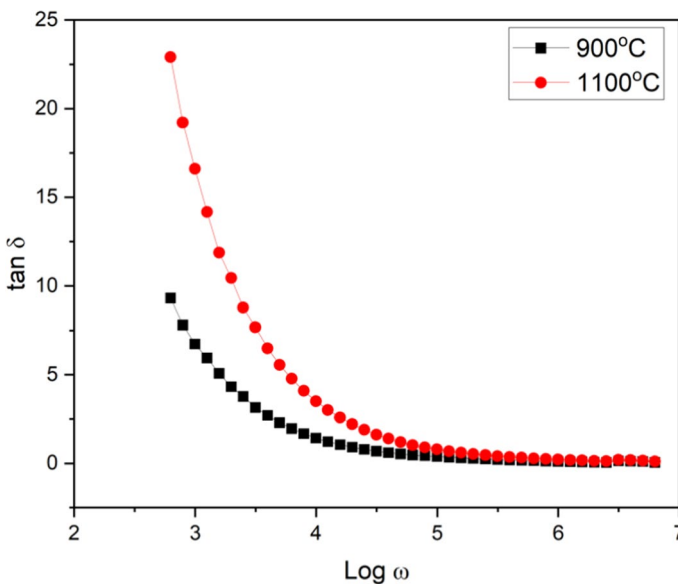


Fig. 13 Variation of dielectric loss tangent ( $\delta$ ) with frequency

### 5.4 Complex modulus

Complex modulus ( $M$ ) spectroscopy is an important technique to study the electrical phenomena in dielectric material (Joshi et al. 2017). Complex modulus spectroscopy is advantageous to distinguish between electrode polarization and conduction due to grain boundary. The electric modulus is expressed as

$$M^* = M' - iM'', M' = \frac{\epsilon I}{\epsilon I^2 + \epsilon II^2}, M'' = \frac{\epsilon I}{\epsilon I^2 + \epsilon II^2} \tag{9}$$

where  $M'$  and  $M''$  are the real and imaginary parts of complex modulus. The graph between  $M'$  and  $M''$  is shown in Fig. 14 at 900 °C and 1100 °C. The Fig. 14 shows two semicircle arcs. The semicircle at lower frequency represents the effect of grain and at higher frequency is due to the effect of grain boundaries. The relation of semicircle arc with grain, and grain boundaries, is described in the impedance ( $Z$ ) section.

The insert graph real ( $M'$ ) part of complex modulus with respect to frequency. At low-frequency regions the value of  $M'$  is low and with frequency real modulus ( $M'$ ) increases

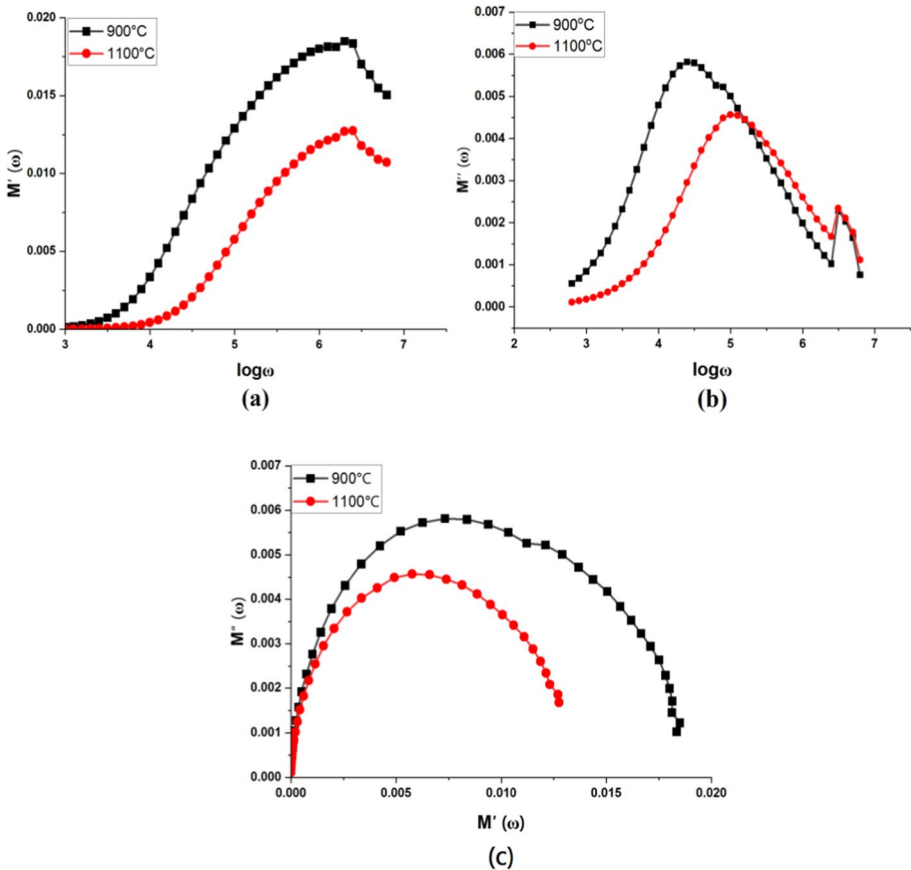


Fig. 14 a Real part of electric modulus, b imaginary part of electric modulus, c complex analysis of electric modulus



and starts to disperse. This type of behavior is due to the reason that at lower frequency region electrode polarization is active. Furthermore the magnitude of  $M''$  decreases with increasing temperature, which may be attributed to a temperature dependent relaxation process. Figure 14 shows the variation of imaginary modulus ( $M''$ ) with frequency. As the sintering temperature increases the relaxation peak ( $M''_{\max}$ ) shifts towards higher frequency due to correlated motions of mobile ions. The frequency regions below  $M''_{\max}$  determines the range in which charge carrier are mobile on long distance and above  $M''_{\max}$  the charge carriers are confined to potential well and remain mobile for shorter distance (Lazanas and Mamas 2023; Sahu and Agrawal 2023).

Figure 15 shows the variation of  $Z''$  and  $M''$  w.r.t frequency at 1100 °C. It is seen that both the peaks  $Z''$  and  $M''$  do not overlap with each other indicating the non-Debye relaxation behavior. This type of behavior indicates that the sample contains components of both from long range conductivity to short range relaxation.

## 6 Conclusion

Magnesium aluminate spinel was synthesized by sol-gel route. XRD studies confirm the FCC cubic spinel-type structure of  $MgAl_2O_4$  and had crystallite size found to be 22 nm and 49 nm. As the sintering temperature increases, the intensity of diffraction peaks increases indicating the increase in the crystalline nature of the material. The FESEM studies the change in morphology with sintering temperature. The fluorescence spectra show an emission peak at 695 nm which is due to the presence of  $F_2^{1+}$  defect centers. The intensity of this emission peak increases from 900 to 1100 °C. Dielectric studies are carried out in a frequency range of 1–10<sup>6</sup> Hz. The AC conductivity of the material is found to increase with frequency due to the hopping of charges, and grain effect and might be due to a reduction in porosity. The radii of a semicircle of Nyquist plot decreases as sintering temperature rises from 900 to 1100 °C which in turn results in an increasing conductivity of material.

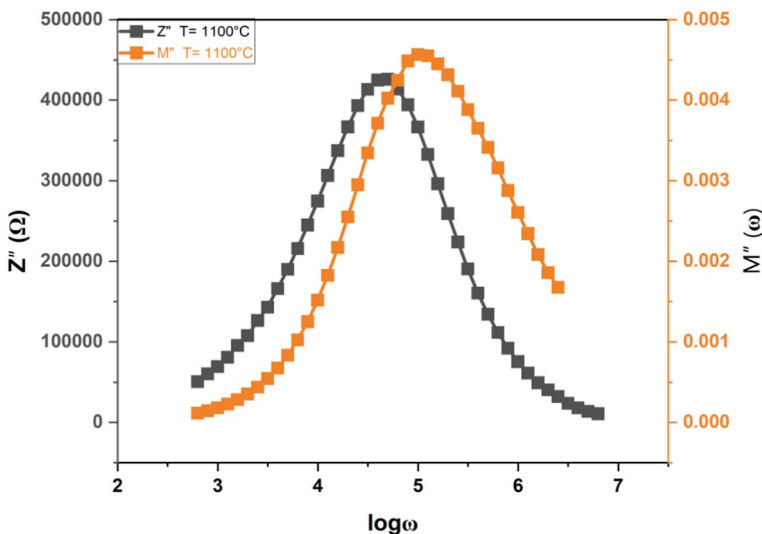


Fig. 15 Shows the variation of  $Z''$  and  $M''$  w.r.t frequency

The Nyquist plot (Cole–Cole) shows the single semicircle providing the LR[Q[R(CR)]] equivalent circuit which corresponds to grain, grain boundary, and electrode contribution. The absence of three separate semicircular arcs is because the bulk, grain boundary, and electrode contributions are not far away. Among the two different temperatures, i.e. at 900 °C and 1100 °C, the optimal sintering temperature is found to be at 1100 °C due to the reason that crystalline nature, FL emission intensity, and AC conductivity increase at this temperature. Furthermore, to improve/enhance these properties suitable dopants can be incorporated. The optical and dielectric properties suggest the probable usage of these nanopowders in optoelectric devices, red-light emitting diodes, high-frequency applications, and storage media.

**Acknowledgements** The authors are thankful to the CIF Lovely Professional University, for providing characterization facility to complete the study.

**Author contributions** Prabhpreet Kaur wrote the initial manuscript. Suman Rani-technical support and finally vetting of paper. All authors reviewed the manuscript.

**Funding** This research received no external funding.

## Declarations

**Competing interests** The authors declare that there is no conflict of interests.

## References

- Ahmed, K., et al.: Enhanced  $\text{Cu}_{2+}$  doping on the structural, optical and electrical properties of zinc oxide (ZnO) nanoparticles for electronic device applications. *J. Lumin.* **250**, 119112–119112 (2022)
- Ali, A., et al.: The effect of Ca dopant on the electrical and dielectric properties of  $\text{BaTi}_4\text{O}_9$  sintered ceramics. *Materials (Basel)* **14**(18), 1–11 (2021)
- Ali, A., et al.: Synthesis and characterizations of  $(\text{Ba}_{1-x}\text{Ca}_x)\text{Ti}_4\text{O}_9$ ,  $0 \leq x \leq 0.9$  ceramics. *J. Mater. Res. Technol.* **11**, 1828–1833 (2021)
- Barik, S.K., Choudhary, R.N.P., Singh, A.K.: Ac impedance spectroscopy and conductivity studies of  $\text{Ba}_{0.8}\text{Sr}_{0.2}\text{TiO}_3$  ceramics. *Adv. Mater. Lett.* **2**(6), 419–424 (2011)
- Costa, M.M., et al.: Impedance and modulus studies of magnetic ceramic oxide  $\text{Ba}_2\text{Co}_2\text{Fe}_{12}\text{O}_{22}$  ( $\text{Co}_2\text{Y}$ ) doped with  $\text{Bi}_2\text{O}_3$ . *J. Appl. Phys.* **110**(3), 1–7 (2011)
- Fayek, M.K.: Effect of Cu substitution on conductivity of Ni–Al ferrite. *J. Phys. Chem. Solids* **61**(9), 1529–1534 (2000)
- Hinklin, T.R., Laine, R.M.: Synthesis of metastable phases in the magnesium spinel– alumina system. *Chem. Mater.* **20**(2), 553–558 (2008)
- Hona, R.K., Dhaliwal, G.S., Thapa, R.: Investigation of grain, grain boundary, and interface contributions on the impedance of  $\text{Ca}_2\text{FeO}_5$ . *Appl. Sci.* **12**(6), 2930–2930 (2022)
- Jagadeeshwaran, C., Madhan, K., Murugaraj, R.: Size effect and order-disorder phase transition in  $\text{MgAl}_2\text{O}_4$ : synthesized by co-precipitation method. *J. Mater. Sci. Mater. Electron.* **29**(22), 18923–18934 (2018)
- Jamal, E.M.A., Kumar, D.S., Anantharaman, M.R.: On structural, optical and dielectric properties of zinc aluminate nanoparticles. *Bull. Mater. Sci.* **34**(2), 251–259 (2011)
- Jameel, M.H., et al.: A comparative study on characterizations and synthesis of pure lead sulfide (PbS) and Ag-doped PbS for photovoltaic applications. *Nanotechnol. Rev.* **10**(1), 1484–1492 (2021a)
- Jameel, M.H., et al.: First principal calculations of electronic, optical and magnetic properties of cubic  $\text{K}_{1-x}\text{Y}_x\text{NbO}_3$  ( $\text{Y} = \text{Fe}, \text{Ni}$ ). *Phys. Scr.* **96**(12), 125839–125839 (2021b)
- Jameel, M.H., Sufi bin Roslan, M., Bin Mayzan, M.Z.H., Agam, M.A.B., Zaki, Z.I., Fallatah, A.M.: Investigation of structural, electronic and optical properties of two-dimensional  $\text{MoS}_2$ -doped- $\text{V}_2\text{O}_5$  composites for photocatalytic application: a density functional theory study. *R. Soc. Open Sci.* **10**(7), 230503–230503 (2023a)

- Jameel, M.H., Roslan, M.S.B., Agam, M.A.B., Alshahrani, T., Alshahrani, B.: Effect of external static pressure on structural, electronic, and optical properties of 2-D hetero-junction MoS<sub>2</sub> for a photocatalytic applications: a DFT study. *Opt. Quantum Electron.* **55**(7), 619–619 (2023b)
- Jameel, M.H., et al.: A comparative DFT study of electronic and optical properties of Pb/Cd-doped LaVO<sub>4</sub> and Pb/Cd-LuVO<sub>4</sub> for electronic device applications. *Comput. Condens. Matter.* **34**, e00773–e00773 (2023c)
- Jian, Q., Wen, Y.: Mechanical and dielectric properties of porous magnesium aluminate (MgAl<sub>2</sub>O<sub>4</sub>) spinel ceramics fabricated by direct foaming-gelcasting. *Ceram. Int.* **46**(2), 1442–1447 (2020)
- Joshi, J.H., et al.: Dielectric relaxation, complex impedance and modulus spectroscopic studies of mix phase rod like cobalt sulfide nanoparticles. *Mater. Res. Bull.* **93**, 63–73 (2017)
- Justin, P., Rao, G.R.: CoS spheres for high-rate electrochemical capacitive energy storage application. *Int. J. Hydrog. Energy* **35**(18), 3–9 (2010)
- Kaur, P., Rani, S.: Effect of sintering temperature on structural and optical properties of magnesium aluminate spinel. *J. Opt.* **52**(4), 2366–2374 (2023)
- Kumar, S.A., et al.: Enhanced power conversion efficiency of the polycrystalline solar cells using spinel MnFe<sub>2</sub>O<sub>4</sub> nanoparticles as an ARC material. *J. Ovonic Res.* **17**(5), 421–427 (2021)
- Lazanas, A.C., Mamas, I.P.: electrochemical impedance spectroscopy-A tutorial. *ACS Meas. Sci. Au.* (2023)
- Li, X., et al.: Improved microwave dielectric properties of MgAl<sub>2</sub>O<sub>4</sub> spinel ceramics through (Li<sub>1/3</sub>Ti<sub>2/3</sub>)<sup>3+</sup> doping. *Chin. Phys. B* **32**(5), 5057701–5057701 (2023)
- Manohar, A., Vijayakanth, V., Prabhakar, S.V., Kim, K.H.: Structural and electrochemical properties of mixed calcium-zinc spinel ferrites nanoparticles. *Ceram. Int.* **49**(3), 4365–4371 (2022)
- Mohan, U., Gogoi, P., Baruah, S.K.: Impedance spectroscopy study of the AC conductivity and dielectric properties of 3, 5-dimethylpyridine-iodine charge transfer complex. *Orient. J. Chem.* **32**(2), 1003–1014 (2016)
- Mostafa, M.M.M., et al.: Electrochemical characteristics of nanosized Cu, Ni, and Zn cobaltite spinel materials. *Catalysts* **12**(8), 893–893 (2022)
- Panda, R.K., Behera, D.: Investigation of electric transport behavior of bulk CoFe<sub>2</sub>O<sub>4</sub> by complex impedance spectroscopy. *J. Alloys Compd.* **587**, 481–486 (2014)
- Pathak, N., et al.: defects induced changes in the electronic structures of MgO and their correlation with the optical properties: a special case of electron-hole recombination from the conduction band. *RSC Adv.* **6**(98), 96398–96415 (2016)
- Pathak, N., et al.: Exploring defect-induced emission in ZnAl<sub>2</sub>O<sub>4</sub>: an exceptional color-tunable phosphor material with diverse lifetimes. *Inorg. Chem.* **57**(7), 3963–3982 (2018)
- Rao, B.N., Rao, P.T., Basha, S.E., Prasanna, D.S.L., Samatha, K., Ramachandra, R.K.: Optical response of Eu<sup>3+</sup>-activated MgAl<sub>2</sub>O<sub>4</sub> nanophosphors for Red emissive. *J. Mater. Sci. Mater. Electron.* **34**(11), 955–955 (2023)
- Rébola, A., Fong, D.D., Eastman, J.A., Ögüt, S., Zapol, P.: First-principles study of compensation mechanisms in negatively charged LaGaO<sub>3</sub>/MgAl<sub>2</sub>O<sub>4</sub> interfaces. *Phys. Rev. B* **87**(24), 245117–245117 (2013)
- Sahu, Y., Agrawal, S.: Structural features, dielectric behaviour of spinel type magnesium aluminate synthesized by the auto-combustion method. *J. Phys. Conf. Ser.* **2576**(1), 012006–012006 (2023)
- Saleem, S., et al.: Evaluation of structural, morphological, optical, and electrical properties of zinc oxide semiconductor nanoparticles with microwave plasma treatment for electronic device applications. *J. Mater. Res. Technol.* **19**, 2126–2134 (2022a)
- Saleem, S., et al.: Modification in structural, optical, morphological, and electrical properties of zinc oxide (ZnO) nanoparticles (NPs) by metal (Ni, Co) dopants for electronic device applications. *Arab. J. Chem.* **15**(1), 103518–103518 (2022b)
- Saleem, S., et al.: Enhancement in structural, morphological, and optical properties of copper oxide for optoelectronic device applications. *Nanotechnol. Rev.* **11**(1), 2827–2838 (2022c)
- Sharma, A., Godara, S.K., Srivastava, A.K.: Influence of composition variation on structural, magnetic and dielectric. *Ind. J. Phys.* **96**(14), 4173–4184 (2022)
- Shi, Z., Zhao, Q., Guo, B., Ji, T., Wang, H.: A review on processing polycrystalline magnesium aluminate spinel (MgAl<sub>2</sub>O<sub>4</sub>): sintering techniques, material properties and machinability. *Mater. Des.* **193**, 108858–108858 (2020)
- Sun, Y., et al.: Navigating surface reconstruction of spinel oxides for electrochemical water oxidation. *Nat. Commun.* **14**(1), 1–11 (2023)
- Thibaudau, P., Gervais, F.: Ab initio investigation of phonon modes in the MgAl<sub>2</sub>O<sub>4</sub> spinel. *J. Condens. Matter Phys.* **14**(13), 3543–3543 (2002)

Zayani, W., et al.: Electrochemical behavior of a spinel zinc ferrite alloy obtained by a simple sol-gel route for Ni-MH battery applications. *Int. J. Energy Res.* **45**(4), 5235–5247 (2021)

**Publisher's Note** Springer Nature remains neutral with regard to jurisdictional claims in published maps and institutional affiliations.

Springer Nature or its licensor (e.g. a society or other partner) holds exclusive rights to this article under a publishing agreement with the author(s) or other rightsholder(s); author self-archiving of the accepted manuscript version of this article is solely governed by the terms of such publishing agreement and applicable law.